Springer

Journal of
Mechanical
Science and
Technology

Journal of Mechanical Science and Technology 22 (2008) 608~617

www.springerlink.com/content/1738-494x

An experimental study on the distribution of the drop size and velocity in asymmetric impinging jet sprays

Choong Hoon Lee*

Department of Automotive Engineering Seoul National University of Technology Seoul 139-743, Korea

(Manuscript Received July 11, 2007; Revised November 26, 2007; Accepted November 27, 2007)

Abstract

Distributions of the drop size and velocity in an asymmetric impinging jet are investigated by injecting water and a sodium carbonate (Na_2CO_3) solution, which simulates the mixing process in impinging jet sprays of liquid oxidizer and liquid fuel for liquid propellants. The liquid sheet formed from the impinging jet is visualized and the drop size distributions are obtained by using image processing for the visualized images. The drop size distribution of the asymmetric impinging jets is fitted to the Rosin-Rammler distribution function. The obtained drop size distributions according to the azimuth angle in the impinging jet are compared with the theoretical predictions of previous research. The experimental results of the drop size distributions are located between the two curves obtained from the theoretical predictions by treating each jet in the asymmetric impinging jets as an independent wall-impinging jet. PIV images using a double-exposure method were processed to obtain the drop velocity vector in the impinging jets. Whether the drops shedding from the edge of the asymmetric impinging jets occurs radially or tangentially is also investigated from the PIV results.

Keywords: Asymmetric impinging jet; Drop size; Drop velocity; Particle image velocimetry

1. Introduction

The sprays formed by two impinging liquid jets are widely used in the supply of liquid fuel and oxidizer in liquid propellant rocket combustors. The liquid jets from two nozzles impinge upon each other to form a liquid sheet. At low velocities, the spray from the impinging jets is patterned into stable liquid sheets that shed drops at the edges of the sheets. When the liquid is transported towards the edge of a sheet, the thickness decreases and disturbances are amplified. When the surface tension and inertia become unbalanced, ligaments are formed and droplets are then generated [1].

The shape and thickness of the impinging jets and the distribution of the drop size and velocity of the sprays were investigated by Ranz [2], Hasson and Peck [3], Kang et al. [4] and Choo and Kang [5] with a stable liquid sheet with relatively low jet velocities. Couto and Bastos-Netto [6] and Ibrahim and Przekwas [7] investigated the atomization characteristics of impinging jets experimentally. Ashgriz et al. [8] investigated the mixing characteristics of sprays formed by the impingement of two water jets, and Lee et al. [9] investigated the mixture composition distribution in asymmetric impinging jets using impinging jets formed by water and a sodium carbonate (Na_2CO_3) solution of which the mixture composition distribution was measured with an acid-base titration technique. Jung [10] et al. measured the mass concentration and mass flux of the impinging jets using the PLIF technique.

In practical combustors, the fuel and oxidizer must be miscible and supplied in a near-stoichiometric proportion. Therefore, the two impinging jets can be asymmetric. However, most research related to impinging jets, with a small number of exceptions, has

*Corresponding author. Tel.: +82 2 970 6393, Fax.: +82 2 979 7032
E-mail address: chlee5@snut.ac.kr
DOI 10.1007/s12206-007-1114-6

focused on symmetric impinging jets. Scant research exists regarding the distribution of the drop size and velocity in asymmetric impinging jets. In the present study, the distribution of the drop size and velocity in impinging jets are investigated by using a miscible water and sodium carbonate (Na_2CO_3) solution. The water and the sodium carbonate in the solution simulate the oxidizer and the fuel, respectively. An existing model [11] for a wall jet was adopted to calculate the predicted theoretical drop size distribution of the asymmetric impinging jets in which each jet is treated as a wall-impinging jet. Captured camera images using a double-exposure method were processed to track the location of each drop. The location was then used to calculate the drop velocity vectors in the impinging jets.

2. Experiment

The experimental setup consists of pressurized vessels for the compressing liquid, flow control system, nozzles and their positioners. The liquid vessels for water and 1 M (Molarity) sodium carbonate (Na_2CO_3) solution were pressurized at 2 atm by using regulated compressed air. Variable-area flow meters were used for the flow rate control. The nozzle consisted of a stainless steel tube with an inner diameter of 0.67 mm. The tubes were long enough to attain fully developed flow at the nozzle exits.

The liquid sheet and droplet-formation processes in the asymmetric impinging jets were visualized with a 35-mm film camera and a stroboscope. The camera and stroboscope were positioned opposite to each other with the liquid sheet in between. Thus, the images captured are forward scattering images of the impinging jets. A double-exposure image that tracked each drop was captured. By setting the shutter speed of the camera at 1/500 sec, the camera film was exposed to the stroboscope light source, which was adjusted to generate a pulse of light with a frequency of 1000 Hz. The film was exposed to two consecutive pulses of the stroboscope in each trial, as the time interval between the two consecutive pulses of the stroboscope was 1/1000 second.

Fig. 1 shows a schematic of the asymmetric impinging jets and various geometric notations. The nozzles are aligned in the *y*-*z* plane and liquid sheets are formed in the *x*-*z* plane. The injection angles of water and sodium carbonate solution jets relative to the *z*-axis are defined as θ_w and θ_s, respectively. Here,

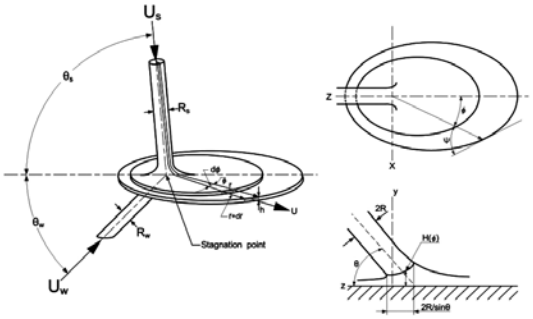

Fig. 1. Schematic diagram of the liquid sheet formed by the impinging jets.

the subscripts *w* and *s* indicate water and sodium carbonate solution, respectively, and $\theta = \theta_w + \theta_s$ is defined as the impinging angle. For a specified impinging angle, the two injection angles are determined from the momentum balance in the *y*-direction [12] and the liquid sheet that forms is then aligned in the *x*-*z* plane.

In the present study, the distribution of the drop size and the velocity are investigated while the ratio of mass flow rate $m_w : m_s$, and the impinging angle θ was changed. The density, the viscosity and the surface tension of the water are ρ_w =1.0 (g/cm^3), σ_w = 0.073 (N/m) and ν_w = 0.01 (cm^2/s), respectively. The density, the viscosity and the surface tension of the sodium carbonate solution are ρ_s = 1.1 (g/cm^3), σ_s = 0.70 (N/m) and ν_s = 0.012 (cm^2/s), respectively. The kinematic viscosity and surface tension of the sodium carbonate solution were determined from a pressure drop through a capillary and by measuring the vertical height and contact angle of the liquid in the capillary tube that was vertically immersed in the solution reservoir, respectively.

3. Image processing

The distribution of the drop size was obtained via image processing of a captured image of the impinging jets. The software used for this step was NI-Vision^{TR}. The original image was processed with a script file consisting of several steps of the image processing functions. Fig. 2 describes the processing of the images. The image in Fig. 2 (a) is the original captured image. The first step in the processing of this image involves edge detection, which finds edges along a selected path based on the threshold of the grayscale values, as shown in Fig. 2 (b). In this study, a Sobel filter was used as a high-pass filter that ex-

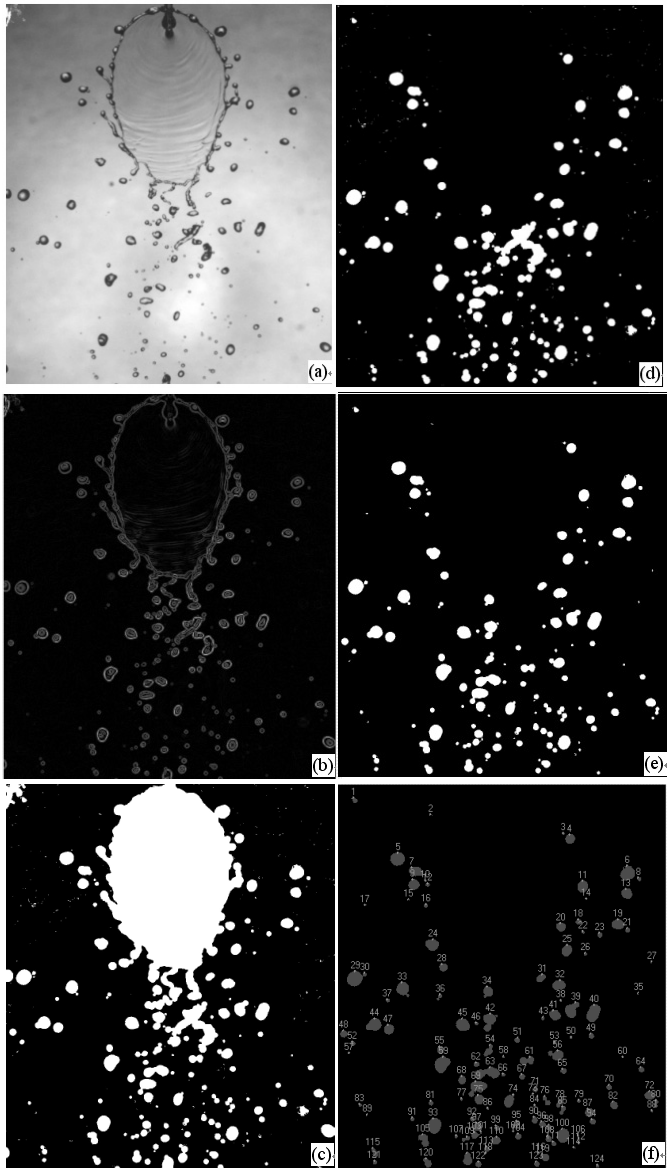

Fig. 2. Image-processing steps for obtaining the distribution of the drop sizes in typical impinging jets.

tracts the outer contours of objects. The next step is to close the borders of the particles and fill the holes, as shown in Fig. 2 (c). Fig. 2 (d) shows the process of selecting actual drops by removing the shape of the borders. Tiny particles that are not drops but noises are then removed by a particle filter, as shown in Fig. 2 (e). Fig. 2 (f) displays the final results for selected particle measurements performed on the aforementioned image with assigning numeric labels for each drop.

Fig. 3 shows the image processing steps necessary to obtain the velocity distribution of drops shed from the impinging jets. Double exposure for the impinging jets was performed to obtain a PIV image of the impinging jets. The velocity of the drops was calculated from dividing the moving distance between a pair of drops by the exposure time of Δt=1ms. Fig. 3 (a) is the original image captured by the double-exposure method. The image processing steps shown in Fig. 3 are similar to those outlined in Fig. 2. A data file that includes the drop size, x-y location and label for each of the drops in Fig. 3 (f) was obtained with

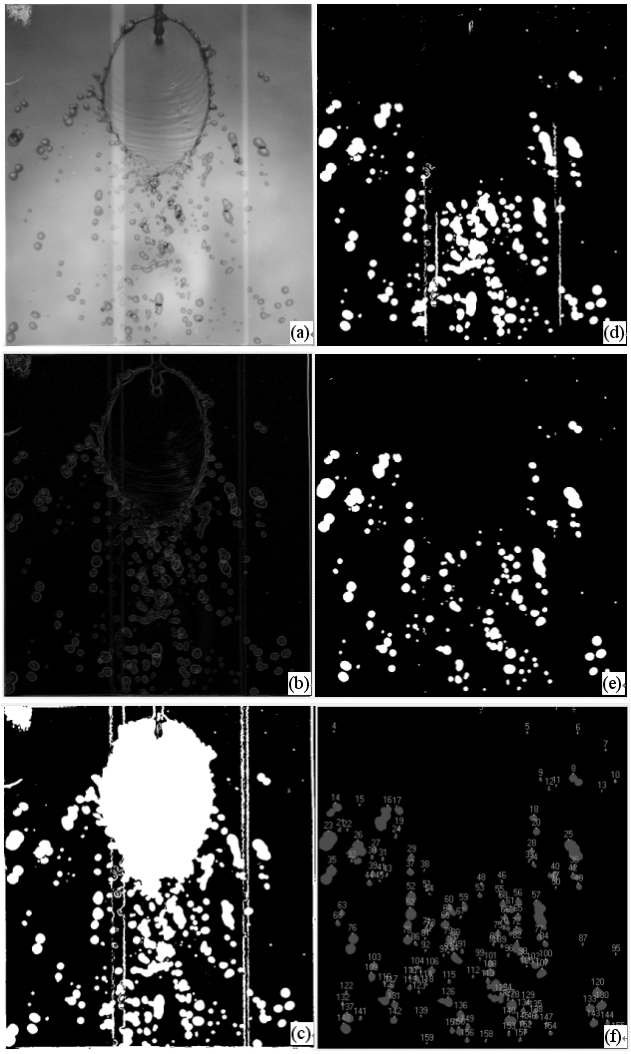

Fig. 3. Image processing steps for obtaining the velocity vectors of the drops from a typical double-exposure image.

the NI-Vision[TR] software. The moving distance between a pair drops during the exposure time could be calculated from the location information contained in the data file. As the number of drops formed from the impinging jets was not great, matching of pairs of drops was performed by comparing the location, size, and direction of the drops one by one in the IDE (integrated development environment) of the NI-Vision[TR] software.

4. Theoretical models to predict the distribution of the drop size

The theoretical distribution of the drop size shed from the symmetric impinging jets was derived by Dombrowski and Johns [13], as follows:

$$d_d = \left(\frac{3\pi}{\sqrt{2}}\right)^{1/3} d_L \left[1 + \frac{3\mu}{\left(\rho_L \sigma d_L\right)^{1/2}}\right]^{1/6} \quad (1)$$

Here, μ (cp), σ (dyn·cm^{-1}) and ρ_L (g·cm^{-3}) are the viscosity, the surface tension, and the liquid density, respectively and d_L (cm) is the ligament diameter following Couto et al. [14]:

$$d_L = 0.9614\left[\frac{K^2\sigma^2}{\rho\rho_L U^4}\right]^{1/6}\left[1 + 2.60\mu^3\sqrt{\frac{K\rho^4U^7}{72\rho_L{}^2\sigma^5}}\right]^{1/5} \quad (2)$$

Here, ρ (g·cm^{-3}) is the density of the gaseous me-

dium, U can be considered nearly equal to the jet velocity, and K is written as in Couto et al. [14],

$$K = \frac{R^2 \sin^3 \theta}{(1 - \cos\phi \cos\theta)^2} \tag{3}$$

In Eq. (3), R represents the radius of the liquid jet, θ is the impinging angle, and ϕ is the azimuth angle of the impinging sheet. By substituting Eq. (2) and Eq. (3) into Eq. (1), the theoretical drop size distribution according to the azimuth angle can be calculated for symmetric impinging jets. The ratio of the mass flow rate of m_w:m_s was varied as 1:1, 1.4:1 and 2:1. The impinging jets formed with the condition of m_w:m_s = 1:1, which is symmetric only when the ratio of the mass flow rate is asymmetric, as the properties (densities) of the water and sodium carbonate solution differ, which results in two different impinging angles θ_w, θ_s, respectively.

For these asymmetric jets, the water jet and sodium carbonate solution jet are treated separately in the estimation of the theoretical drop distribution. Lee et al. [9] applied the wall-impinging jet model of Reitz and Naber [11] to calculate the flow rate of each jet in asymmetric impinging jets. Similarly, the jets of the present asymmetric impinging jets are treated as a wall-impinging jet in which each jet has a wall-impinging angle characterized by θ_w and θ_s, as defined in Fig. 1. The theoretical drop distribution for each jet in the asymmetric impinging jets can be calculated by applying a symmetric model to each jet, as characterized by θ=2θ_w and θ=2θ_s for the impinging angle.

5. Results and discussion

The steps of the image processing as shown in Fig. 2 were applied to the original film image. The locations and sizes of the drops were obtained by assigning numeric labels for each drop, as shown in Fig. 2 (f). The Rosin-Rammler distribution function [15] was compared to the size distribution of the drops in the impinging jets. The Rosin-Rammler distribution is expressed as follows:

$$1 - Q = \exp -(D/X)^q \tag{4}$$

Here, Q is the volume fraction of the drops whose diameter is less than D, q is an adjustable constant that functions to improve the fit to experimental data, and X is the drop diameter such that 63.2 % of the total liquid volume is in drops of a smaller diameter.

Figs. 4-6 show the cumulative volume fraction of the experimental drop size distributions in a comparison with the Rosin-Rammler distribution function. Here, the ratio of the mass flow rate and the impinging angle of the impinging jets varies. The Rosin-Rammler distribution model fits comparatively well the experimental results; the sizes of the drops are distributed in an approximate range of 150 μm to 3000 μm. Fig. 4 shows the results for the impinging jets with a ratio of the mass flow rate of m_w:m_s = 1:1 and impinging angles (a) θ=90˚ (θ_w=42˚, θ_s=48˚), and (b) θ=120˚ (θ_w=52˚, θ_s=68˚). The Reynolds number of each jet at conditions of θ =90˚ and θ=120˚ is Re_w=2870 and Re_s=1690, respectively.

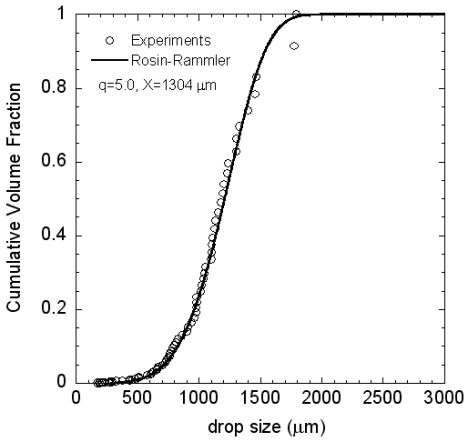

(a)

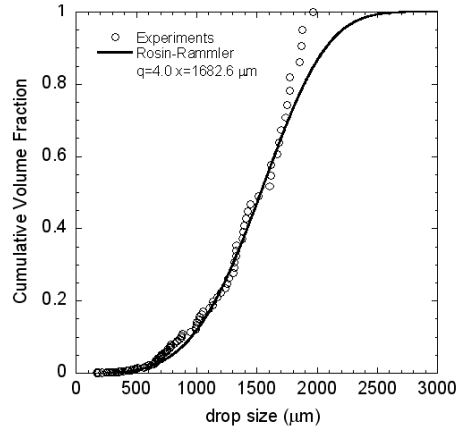

(b)

Fig. 4. Comparison of the experimental drop size distribution obtained from the processing of the image with the Rosin-Rammler model for m_w:m_s=1:1 ; (a) θ=90˚ and (b) θ=120˚.

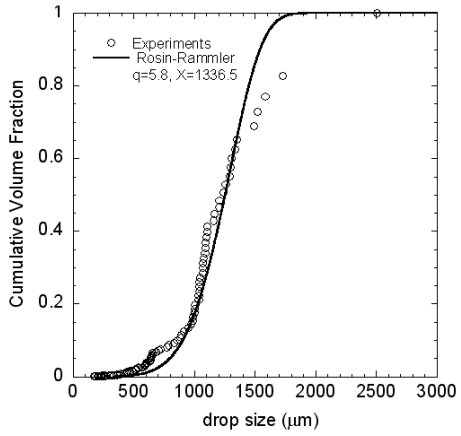

(a)

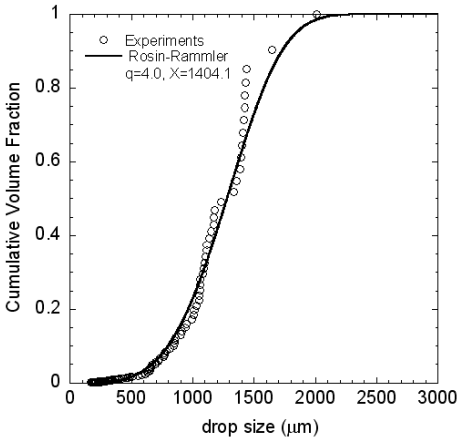

(b)

Fig. 5. Comparison of the experimental drop size distribution obtained from the processing of the image with the Rosin-Rammler model for m_w:m_s = 1.4:1 ; (a) θ = 90˚ and (b) θ = 120˚.

Fig. 5 shows the results for the impinging jets with the ratio of the mass flow rate of m_w:m_s = 1.4:1 and the impinging angles (a) θ = 90˚ (θ_w =25˚, θ_s =65˚), and (b) θ = 120˚ (θ_w =31˚, θ_s =89˚). The Reynolds number of each jet in both the θ =90˚ and θ=120˚ cases is Re_w=4010 and Re_s=1690, respectively. The distribution of the drop size for θ=120˚ is similar to that at θ=90˚. The distribution of the drop size with a ratio of the mass flow rate of m_w:m_s = 1.4:1 is smaller than that with a ratio of the mass flow rate of m_w:m_s = 1:1 due to the higher velocity of the water jet with a ratio of the mass flow rate of m_w:m_s = 1.4:1. Fig. 6 shows the results for the impinging jets with a ratio of the mass flow rate of m_w:m_s = 2:1 and the impinging angle θ= 90˚ (θ_w =13˚, θ_s =77˚). The Reynolds num-

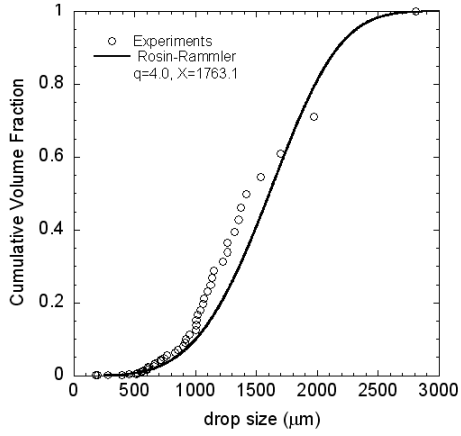

Fig. 6. Comparison of the experimental drop size distribution obtained from the processing of the image with the Rosin-Rammler model for m_w:m_s=2:1, θ=90˚.

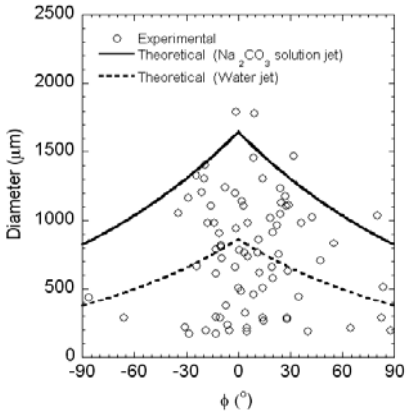

(a) θ=90˚

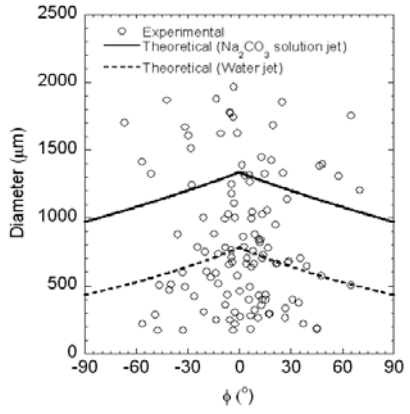

(b) θ=120˚

Fig. 7. Experimental drop size distribution of the impinging jets according to the azimuth angle and a comparison with the theoretical predictions for m_w:m_s=1:1 ; (a) θ=90˚ and (b) θ=120˚.

ber for the two jets with a ratio of the mass flow rate of m_w:m_s=2:1 is Re_w=4880 and Re_s=1420, respectively.

The distribution of the drop size according to the azimuth angle was compared with the theoretical calculations of Dombroski and Johns [13] and with the K value from Couto et al. [14]. Fig. 7 shows a comparison of the results between the experiments and theoretical predictions while varying the azimuth angle ϕ for the ratio of the mass flow rate of m_w:m_s = 1:1 and the impinging angles (a) θ=90˚ (θ_w=42˚, θ_s=48˚), (b) θ=120˚ (θ_w=52˚, θ_s=68˚), respectively. The circle in Fig. 7 represents the experimental results, and the solid and dashed lines in Fig. 7 represent theoretical predictions of the drop size distribution for the sodium carbonate solution and water jets, respectively. The experimental drop sizes were distributed ranging from 150 μm to 2000 μm; they decrease as the azimuth angle increases. The theoretical predictions of the sodium carbonate solution jet are larger than those of the water jet due to the lower jet velocity of the sodium carbonate solution. The solid line and dashed line in Fig. 7 represent the upper and lower limits, respectively, of the theoretical predictions in the drop sizes of the asymmetric impinging jets, and the prediction of the drop size decreases as the azimuth angle increases. This is in good agreement with trends in the experimental results. The experimental drop sizes are distributed over both the solid line and dashed line and are comparatively well fitted to the ranges of theoretical predictions. The Reynolds numbers of each jet in both the θ=90˚ and θ=120˚ cases are identical to Re_w=2870, Re_s=1690, respectively. The larger jet angles θ_s=68˚ and θ_w= 52˚of the sodium carbonate solution and the water jet at θ=120˚ cause a wider drop distribution over the azimuth angle as well as an increase in the number of drops due to the greater impinging momentum of the impinging jets compared to those at θ=90˚.

Fig. 8 shows for the results with the ratio of the mass flow rate of m_w:m_s = 1.4:1 and the impinging angles (a) θ=90˚ (θ_w=25˚, θ_s=65˚), and (b) θ=120˚ (θ_w=31˚, θ_s=89˚). The results are similar to those of the mass flow rate ratio of m_w:m_s = 1:1, as shown in Fig. 7. Fig. 9 shows the results for a ratio of the mass flow rate of m_w:m_s = 2:1 and impinging angle of θ=90˚ (θ_w=13˚, θ_s=77˚). The results are also similar to those of the mass flow rate ratio of m_w:m_s = 1.4:1. In case of an impinging angle of θ=120˚ with a mass flow rate ratio of m_w:m_s = 2:1, the liquid sheet did not form.

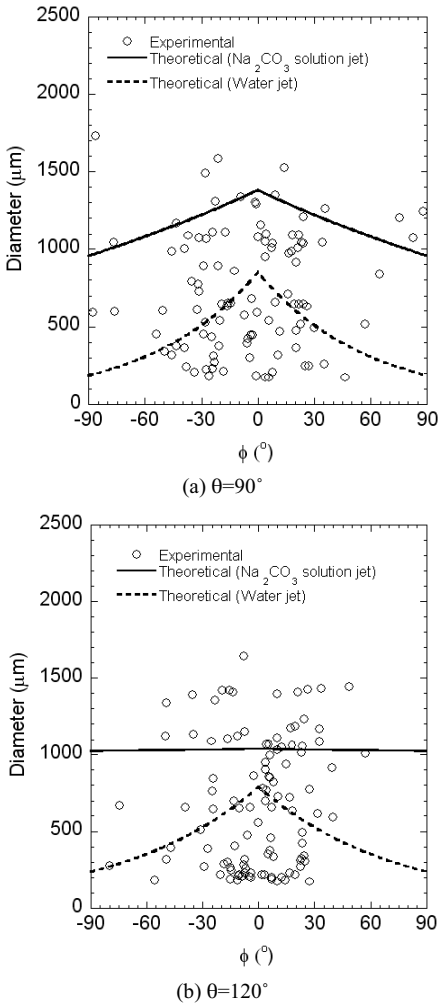

Fig. 8. Experimental drop distribution of the impinging jets according to the azimuth angle and a comparison with the theoretical predictions for m_w:m_s = 1.4:1 ; (a) θ = 90˚ and (b) θ = 120˚.

In Figs. 7 and 8, the theoretical drop size distributions generally fail to account for the wide distribution of droplet sizes, ranging from 200 μm to 2000 μm. Kang et al. [4] explained that this discrepancy could come from the assumption of Dombrowski and Johns [14] that only one size of droplets is created from the unstable liquid ligaments. A more improved theoretical model which includes the generation of multiple sizes of droplets should be developed to enhance the accuracy of the theoretical prediction.

The image processing steps that obtain the velocity distribution of drops shed from the impinging jets (explained previously) were applied to a double-exposure image of the impinging jets. Figs. 10-12

show the velocity vector of the drops shed from the impinging jets by connecting every location of the drops that moves during the 1-ms double-exposure time interval with the varying ratios of the mass flow rate of m_w:m_s = 1:1, 1.4:1 and 2:1. The small solid circle on the upper side of Figs. 10-12 represents the impinging point of the jets. The circle diameter of each drop represents the detected diameter of the drops obtained from the image processing. The length scale of 0.5 cm is also displayed to aid the estimation of the drop velocity. The velocity of each drop could be calculated by dividing the length of the arrow by the time interval of the double exposure, Δt=1ms. If the length of the arrow of a drop vector is 0.5 cm, the velocity of the drop is 5 m/s. The velocity of each drop shows a distribution of approximately 4 m/s ~ 2 m/s. The velocity vectors of the drops in Figs. 10-12 show a generally symmetric appearance with respect to the z-axis. Each drop generally appears to be directed radially out from the impinging point, as suggested by Taylor [16]. However, a small number of drops have negative velocity vector in the right half of the sheet in the vicinity of ϕ=0˚ and a positive velocity vector in the left hand sheet in the same vicinity. Kang et al. [4] explained these characteristics of the velocity vector in the vicinity of ϕ=0˚ as the drops shed from the edges of the impinging jets that occur tangentially along the edge and not radially. Following an analysis of the results of Kang et al. [4] involving symmetric impinging jets, the drops shed from the asymmetric impinging jets in the present study could also occur tangentially along the edge. Whether the droplets shedding from the liquid sheet are to move radially or tangentially is important, because the velocity vector of the droplets which are shedding from the edge of the liquid sheet is used to predict the drop location and mixing characteristics of the impinging jets. The asymmetric impinging jets show similar pattern of the velocity distribution in the symmetric impinging jets investigated by Kang et al. [4].

Fig. 10 shows the velocity vector of drops shed from the impinging jets by connecting each location of the drops that move during the 1-ms double-exposure interval time with a ratio of the mass flow rate of m_w:m_s = 1:1 and the impinging angles of (a) θ=90˚ (θ_w=42˚, θ_s=48˚), and (b) θ=120˚ (θ_w=52˚, θ_s=68˚). The velocity distribution with the impinging angle of θ=90˚ is more uniform compared to that of θ=120˚. This result might be due to the larger difference between θ_w=52˚ and θ_s=68˚ in the impinging jet with θ=120˚, which increases the instability in the liquid sheet of the impinging jets.

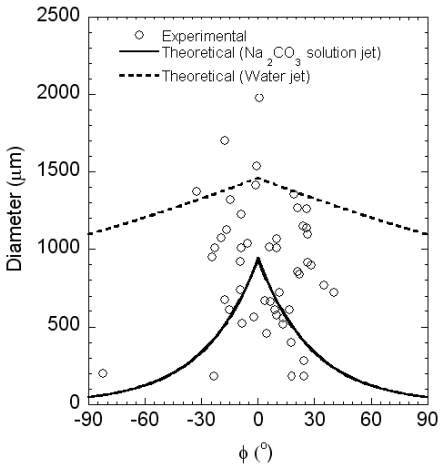

Fig. 9. Experimental drop distribution of the impinging jets according to the azimuth angle and a comparison with the theoretical predictions for m_w:m_s = 2:1, θ = 90˚.

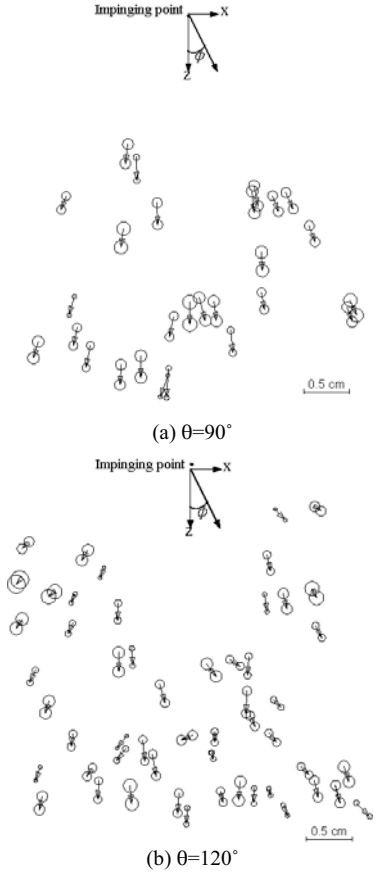

Fig. 10. PIV results for the asymmetric impinging jets for m_w:m_s = 1:1 ; (a) θ = 90˚ and (b) θ = 120˚.

(a) θ=90˚

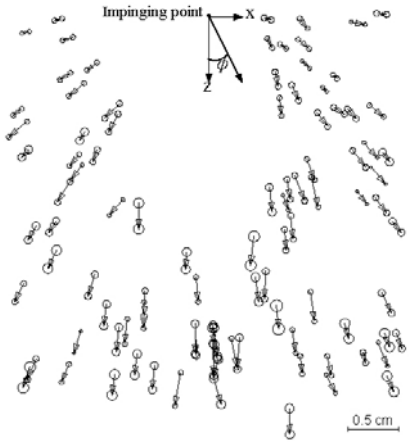

(b) θ=120˚

Fig. 11. PIV results for the asymmetric impinging jets for m_w:m_s = 1.4:1 ; (a) θ = 90˚ and (b) θ = 120˚.

Fig. 11 shows the PIV results, which are similar to those in Fig. 10, with the ratio of mass flow rate of m_w:m_s = 1.4:1 and the impinging angles (a) θ=90˚ (θ_w=25˚, θ_s=65˚), (b) θ=120˚ (θ_w=31˚, θ_s=89˚), respectively. The results shown in Fig. 11 are fairly similar to those in Fig. 10. The velocity of each drop shows a distribution of approximately 3 m/s ~ 5 m/s, which is higher than that with a mass ratio of m_w:m_s = 1:1 due to the larger Reynolds number of Re_w=4010; in other words, this is due to the higher water jet velocity.

Fig. 12 shows the results with a ratio of the mass flow rate of m_w:m_s = 2:1 and the impinging angle of θ=90˚ (θ_w=13˚, θ_s=77˚). Additionally, the results are similar to those with a mass flow rate ratio of m_w:m_s = 1.4:1.

Fig. 12. PIV results for the asymmetric impinging jets for m_w:m_s = 2:1, θ = 90˚.

6. Concluding remarks

Distributions of the drop size and velocity in an asymmetric impinging jet are investigated by using a visualization and image-processing method. An existing model for a wall jet is applied to test the predicted theoretical size distribution of the drops as applied to asymmetric impinging jets.

The experimental results of the drops size obtained from the visualization and image-processing method are in good agreement with the predicted theoretical size distribution using the wall-impinging jet model. The drop velocity distribution in the asymmetric impinging jets from analysis of the PIV images using a double-exposure method show that most drops are shed radially from the asymmetric impinging point except in the vicinity of an azimuth angle of $\phi \approx 0$, in which case a number of drops are shed tangentially along the impinging edge. This is similar to the symmetric impinging jet results.

Nomenclature

d	:	Nozzle diameter (mm)
$H(\phi)$	:	Thickness of liquid sheet at r=R/sinθ
m	:	Mass flow rate (kg/s)
M	:	Molarity
r, R	:	Radius (mm)
Re	:	Reynolds number
U	:	Jet velocity (m/s)
θ_w	:	Injection angle of water jet (˚)
θ_s	:	Injection angle of sodium carbonate (˚)
θ	:	Impinging angle, $\theta = \theta_w + \theta_s$

ρ : Density (g/cm^3)
ν : Kinematic viscosity (cm^2/s)
σ : Surface tension (N/m)
ϕ : Azimuth angle

References

[1] N. D. Dombrowski and P. C. Hooper, A study of the spray formed by impinging jets in laminar and turbulent flow, *J. Fluid Mech*. 18 (1963) 393-400.

[2] W. E. Ranz, Some experiments on the dynamics of liquid films, *J. Appl. Phys.* 30 (1959) 1950-1955.

[3] D. Hasson, and R. E. Peck, Thickness distribution in a sheet formed by impinging jets, *AIChE J*. 10 (1964) 752-754.

[4] B. S. Kang, Y. B. Shen and D. Poulikakos, Holography experiments in the breakup region of a liquid sheet formed by two impinging jets, Atomization and Sprays 5 (1995) 387-402.

[5] Y. J. Choo and B. S. Kang, A study on the velocity distribution of the liquid sheet formed by two impinging jets at low velocities, KSME 2000 Annuals Spring & Fall Conferences 1 (2) (2000) 728-733.

[6] H. S. Couto and D. Basto-Netto, Droplet size distribution from impinging jets, *J. Propulsion and Power* 7 (1991) 654-656.

[7] E. A. Ibrahim, and A. J. Przekwas, Impinging jet atomization, Phys. Fluids A 3 (1991) 2981-2987.

[8] N. Ashgriz, W. Brocklehurst and D. G. Talley, On the mixing mechanisms in a pair of impinging jets, 31st AIAA/ASME/SAE/ASEE Joint Propulsion Conference and Exhibit, July 10-12, (1995) *AIAA paper* 95-2421.

[9] C. H. Lee, Y. H. Jung and S. H. Chung, An experiment on flow distribution and mixing in impinging jet sprays, Atomization and Sprays 9 (1999) 192-213.

[10] K. Jung, H. S. Koh and Y. B. Yoon, Assessment of planar liquid-laser-induced fluorescence measurements for spray mass distributions of like-doublet injectors, Measurement Science Technology 14 (2003) 1387–1395.

[11] J. D. Naber and R. D. Reitz, Modeling engine spray/wall impingement, (1988), SAE Paper 880107.

[12] G. P. Sutton, Rocket Propulsion Elements, John Wiley & Sons (1992).

[13] N. D. Dombrowski and W. R. Johns, The aerodynamic instability and disintegration of viscous liquid sheets, Chemical Engineering Science 18 (1963) 203-214.

[14] H. S. Couto, D. Bastos-Netto and C. E. Migueis, modeling of the initial droplet size distribution function in the spray formed by impinging jets, *Journal of Propulsion*, 8 (3) (1991) 725-728.

[15] A. H. Lefebvre, Atomization and Sprays, Hemisphere Publishing Corporation, (1989).

[16] G. I. Taylor, Formation of thin flat sheets of water, Proc. Roy. Soc. London, 10 (1960) 1-17.